JOURNAL OF Materials CHEMISTRY

Layered double hydroxides with the hydrotalcite-type structure containing Cu^{2+}, Ni^{2+} and Al^{3+}

Vicente Rives*[a] and Srinivasan Kannan[b]

[a]*Departamento de Química Inorgánica, Universidad de Salamanca, 37008-Salamanca, Spain*
[b]*Silicates and Catalysis Discipline, Central Salt and Marine Chemicals Research Institute, Bhavnagar-364 002, India*

Received 25th October 1999, Accepted 6th December 1999

Layered double hydroxides (LDHs) with the hydrotalcite-like structure have been prepared containing different amounts of Ni^{2+}, Cu^{2+} and Al^{3+} in the brucite-like layers by a coprecipitation method. The samples have been characterized by elemental chemical analysis, powder X-ray diffraction, differential thermal analysis and thermogravimetric analysis, FT-IR and UV–VIS diffuse reflectance spectroscopies, temperature-programmed reduction, and specific surface area and porosity assessment by N_2 adsorption at −196 °C. The nature of the phase obtained, crystallinity of the HT-like phase and thermal behaviour of these materials were influenced by M^{II}/Al atomic composition and concentration of bivalent metal ion. Calcination at 500 °C leads to mostly amorphous solids containing NiO, and also CuO (tenorite) for large Cu^{2+} contents (Cu/Ni molar ratio equal to 4). When the calcination temperature is increased to 850 °C, crystallization of well defined phases (NiO, CuO and $NiAl_2O_4$, depending on the relative amounts of Ni, Cu and Al) takes place. Reduction of Cu^{2+} species in these samples takes place at a lower temperature than that for Ni^{2+}, while the temperature of reduction of nickel is increased with an increase in aluminium and copper content of the samples.

Introduction

Hydrotalcites are an example of so-called layered double hydroxides (LDH) or anionic clays, consisting of brucite-like structures, where a partial Mg^{2+}/Al^{3+} substitution has taken place.[1–3] To balance the positive charge in the layers, anions (usually carbonate) are located between the layers, originally occupied by water molecules. The formula of natural hydrotalcite is $Mg_6Al_2(OH)_{16}(CO_3)\cdot 4H_2O$, also written as $[Mg_{0.75}Al_{0.25}(OH)_2](CO_3)_{0.125}\cdot 0.5H_2O$, to emphasize the relationship between the formula and that of brucite, $[Mg(OH)_2]$. In the last decade, materials have been described in the literature where different divalent and trivalent cations have been introduced in the brucite-like layers, and also materials are known with organic anions, oxometalates, anionic metal coordination compounds in the interlayer, *etc.*[1–4]

The nature of the metal cations in the brucite-like layers in synthetic hydrotalcites has been extended in recent years.[1–3] In addition to their intrinsic interest,[2,3] one of the uses of hydrotalcites is as catalyst precursors,[1] as upon calcination or reduction, they lead to well dispersed phases (oxides sometimes known as 'non-stoichiometric spinels' or oxide-supported metallic phases). One of the most widely studied systems corresponds to takovite,[1] a Ni–Al–carbonate LDH. Partial Ni/Mg substitution and addition of other cations have been performed to improve the catalytic activity of the solids obtained upon calcination,[5,6] and the effect of the Ni/Al ratio on the properties of the solids obtained upon calcination has been also reported.[7] However, studies on copper-containing hydrotalcites are scarce in the literature. Wu and coworkers have recently reported[8] the oxidation of phenol on several Cu containing hydrotalcites in the liquid phase. In hydrotalcites containing copper and nickel, reduction to the metallic state can be achieved by treatment with polyols, at temperatures lower than those usually required to reduce them by gaseous hydrogen.[9] Here, we report on the preparation and characterisation of hydrotalcites containing Cu^{2+}, Ni^{2+} and Al^{3+} in the brucite-like layers, as well as on the materials prepared by calcination at different temperatures. These materials are currently under investigation as catalysts for phenol hydroxylation.

Experimental

Sample preparations

All chemicals were from Fluka (Switzerland). The samples were prepared by the low supersaturation technique. A solution (A) containing the desired amount of metal (Ni, Cu, Al) nitrates was mixed with a solution (B) of the precipitating agents (*i.e.*, NaOH and Na_2CO_3). Solutions A and B were added simultaneously, while maintaining the pH around 9–10 under vigorous stirring at room temperature. The addition took *ca.* 90 min and the final pH was adjusted to 10. The samples were aged in the mother-liquor at 65 °C for 24 h, filtered off, washed (until total absence of nitrates and Na in the washing liquids) and dried in an air oven at 80 °C for 12 h. The samples were bluish green, except sample IE6 (see naming below), which was grey.

Techniques

Elemental chemical analysis for Cu, Ni and Al was carried out by atomic absorption in a Mark 2 ELL-240 apparatus, in Servicio General de Análisis Químico Aplicado (University of Salamanca, Spain).

Powder X-ray diffraction (PXRD) patterns were recorded in a Siemens D500 instrument, using Cu-Kα radiation ($\lambda = 1.54050$ Å) and equipped with AT Diffract software. Identification of the crystalline phases were by comparison with the JCPDS files.[10]

FT-IR spectra were recorded in a Perkin-Elmer FT1730 instrument, using KBr pellets; 100 spectra (recorded with a nominal resolution of 4 cm^{-1}) were averaged to improve the signal-to-noise ratio.

UV–VIS spectra were recorded following the diffuse

reflectance (UV–VIS/DR) technique in a Shidmazu UV-240 instrument, using 5 nm slits and MgO as reference.

Temperature-programmed reduction (TPR) analysis was carried out in a Micromeritics 2900 TPD/TPR instrument. The reducing agent was H_2–Ar (5% vol) from L'Air Liquide (Spain) and the gas flow (50 ml min^{-1}), sample weight (10–15 mg) and heating schedule (10 °C min^{-1}) were chosen according to data in the literature[11] to optimize resolution of the curves. Calibration of the instrument was carried out with CuO (from Merck).

Specific surface area assessment and pore size analysis was carried out in a Gemini instrument from Micromeritics. The sample (*ca.* 80–100 mg) was previously degassed in flowing nitrogen at 150 °C for 2 h in order to remove physisorbed water in a FlowPrep 060 apparatus, also from Micromeritics, and the data were analyzed using published software.[12]

Thermogravimetric (TG) and differential thermal analyses (DTA) were carried out in TG-7 and DTA-7 instruments from Perkin Elmer, in flowing oxygen (from Sociedad Española del Oxígeno, Spain), at a heating rate of 10 °C min^{-1}.

Results

Elemental chemical analysis

The results obtained are summarized in Table 1. The formulae calculated for the samples are included in Table 2; the content of carbonate has been calculated from the M^{II} /Al ratio, assuming carbonate is the only interlayer anion balancing the positive charge in the layers because of the presence of aluminium in agreement with results from other experimental techniques (see below); the interlayer water content was calculated from the TG curves.

The M^{II}/Al and Ni/Cu ratios in the solids are in fairly good agreement with the ratios existing in the starting solutions, deviation being in most cases lower than 10%. The lack of coincidence between the initial ratio of cations in the solutions, and the ratio in the solids isolated, is, however, rather common in the literature, and has been usually ascribed to a preferential precipitation of one or another cation as hydroxide.[2]

Powder X-ray diffraction

The powder X-ray diffraction patterns for all six samples are shown in Fig. 1. The patterns for samples IE2–IE6 are typical of a hydrotalcite-like material with intercalated carbonate anions, showing harmonics close to $2\theta = 11$, 24 and 35°, corresponding to basal spacings close to 7.6, 3.8 and 2.6 Å, respectively, ascribed, assuming a 3R packing of the layers,[13,14] to diffraction by planes (003), (006) and (009). The positions of the remaining peaks are in agreement with such an assignment. However, the diffraction pattern of Cu-rich sample (IE6) is relatively broad, especially for higher order reflections, indicating the incompatibility of copper in a regular octahedral network of the hydrotalcite lattice. The first peak of the doublet close to $2\theta = 60$–62° is due to diffraction by planes (110). From the position of this peak, the value of the crystallographic parameter *a* can be calculated by using eqn. (1), while eqn. (2) is used to calculate the value for parameter *c*.[1]

$$a = 2d(110) \quad (1)$$

$$c = d(003) + 2d(006) + 3d(009) \quad (2)$$

The values obtained are included in Table 2 and are in accord with formation of hydrotalcite-like materials; the thickness of the brucite-like layers is *ca.* 4.8 Å,[15] and thus the interlayer space is close to 2.8 Å, suggesting location of carbonate anions with their molecular planes parallel to the brucite-like layers.

The crystallographic parameter *a* equals the average cation–cation distance in the brucite-like layers, which can be estimated from the ionic radii of these cations[16] and their molar fractions in the samples while parameter *c* depends on the thickness of the brucite-like layers, controlled mostly by the size (and orientation) of the interlayer anion and the electrostatic forces operating between the interlayer anion and the layers. It is clear from Table 2 that the lattice parameter *a* increases with an increase in copper content while lattice parameter *c* decreases with an increase in Al content (*i.e.* with

Table 2 Chemical formulae of the samples

Sample	Formula[a]	*c*/Å	*a*/Å
IE2	$[Ni_{0.30}Cu_{0.38}Al_{0.32}(OH)_2](CO_3)_{0.16}\cdot 1.23H_2O$	22.966	3.054
IE3	$[Ni_{0.39}Cu_{0.36}Al_{0.25}(OH)_2](CO_3)_{0.13}\cdot 1.27H_2O$	22.971	3.058
IE4	$[Ni_{0.37}Cu_{0.44}Al_{0.19}(OH)_2](CO_3)_{0.10}\cdot 1.13H_2O$	23.108	3.064
IE5	$[Ni_{0.64}Cu_{0.12}Al_{0.24}(OH)_2](CO_3)_{0.12}\cdot 1.03H_2O$	23.220	3.048
IE6	$[Ni_{0.14}Cu_{0.61}Al_{0.25}(OH)_2](CO_3)_{0.13}\cdot 0.96H_2O$	22.883	3.076

[a]Values have been rounded to two significant figures.

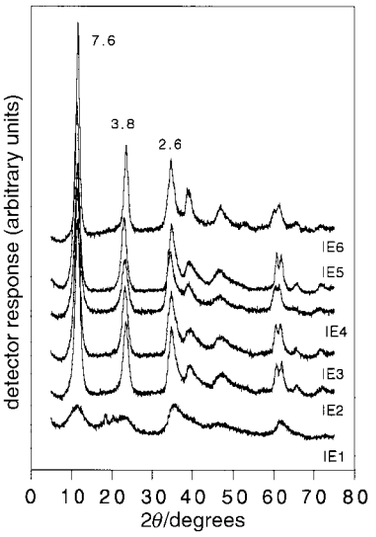

Fig. 1 Powder X-ray diffraction patterns for the samples studied. The curves have been displaced vertically for clarity. Positions marked (Å) correspond to averaged values.

Table 1 Elemental chemical analysis results for the samples

				M^{II}/Al^b		Ni/Cu[b]	
Sample	Ni[a]	Cu[a]	Al[a]	Solution	Solid	Solution	Solid
IE1	13.50	13.24	11.83	1.00	1.00	1.00	1.10
IE2	15.98	22.00	7.68	2.00	2.17	1.00	0.79
IE3	20.63	20.40	6.13	3.00	2.96	1.00	1.09
IE4	19.85	25.63	4.51	4.00	4.44	1.00	0.84
IE5	34.03	6.69	5.87	3.00	3.15	5.00	5.51
IE6	7.53	35.83	6.14	3.00	3.04	0.20	0.23

[a]Weight percentage. [b]Atomic ratio.

an increase in carbonate content). The increase in lattice parameter a can be accounted for by the higher octahedral radius of copper (0.73 Å *cf.* 0.69 Å for nickel), while the decrease in parameter c can be accounted for by a higher electrostatic interaction between the layer and the interlayer.

Considering sample IE1, although its XRD pattern resembles an HT-like phase, the peaks are broad and ill-defined. In addition peaks around $2\theta = 18.30$ and 20.50°, can be ascribed to $Al(OH)_3$, gibbsite (JCPDS file 12-0460). It is known for hydrotalcites, that a composition with an M^{II}/Al atomic ratio of <2.0 leads to a preferential segregation of aluminium as $Al(OH)_3$. Hence, in subsequent discussions, sample IE1 will not be considered.

FT-IR spectroscopy

FT-IR spectra of the samples are shown in Fig. 2. The technique has been used to identify the nature and symmetry of interlayer anions and the presence of impurity phases.

All samples showed a broad intense band between 4000 and 3000 cm^{-1} due to the OH stretching mode of layer hydroxy groups and of interlayer water molecules.[17] Although the position of this band should be dependent on the nature of the layer cation, as its electronegativity will modify the electron density on the O–H bond (M–OH), the extreme broadness of this band, owing to hydrogen bonding, precludes any meaningful discussion. A weak shoulder recorded in some cases (especially for samples IE3 and IE5) around 3000 cm^{-1} has been ascribed[18,19] to the OH stretching mode of interlayer water molecules hydrogen-bonded to interlayer carbonate anions. The bending mode of water molecules is responsible for the weak band at 1640–1620 cm^{-1}. The rather sharp, intense band at 1375–1365 cm^{-1} is due to mode v_3 antisymmetric stretching of interlayer carbonate, shifted from its position in free CO_3^{2-} because of strong hydrogen bonding with hydroxy sheets and H_2O molecules in the interlayer.[17] However for sample IE4, a split in the v_3 vibration is observed (1372 cm^{-1} and 1471 cm^{-1}) with simultaneous detection of a very weak shoulder at 1054 cm^{-1}. This shoulder can be ascribed to the v_1 mode of carbonate; although this mode is IR-inactive in the D_{3h} symmetry of free carbonate, it becomes activated owing to lowering of symmetry of carbonate in the interlayer (probably to C_{3v} or C_{2v}), which is also responsible for splitting of the v_3 band. Displacement and splitting of this band has also been observed in calcite and aragonite, where the local symmetry of carbonate is D_3 and C_s, respectively.[20,21] The bands recorded below 1000 cm^{-1} can be ascribed to mode v_2 of carbonate (*ca.* 850 cm^{-1}) and to M–OH modes.

These results confirm the presence of carbonate, as well as the absence of nitrate, in the interlayer space of the synthesized hydrotalcites. Simultaneous formation of an OH-containing phase LDH (meixnerite) cannot be ruled out, although it is very unlikely because of the known preferential intercalation of carbonate.

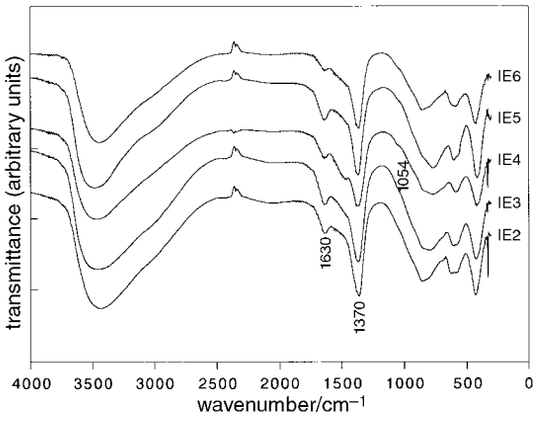

Fig. 2 FT-IR spectra for the samples studied. The curves have been displaced vertically for clarity. Positions marked (cm^{-1}) correspond to averaged values.

UV–VIS spectroscopy

UV–VIS/DR spectra for all samples are shown in Fig. 3. It is clear that the copper rich sample has an absorption maximum around 770 nm while for the Ni-rich sample this is around 660 nm, and for the other samples the absorption maximum lies between these two values. In the UV region, the Ni-rich sample shows a maximum around 300 nm while the Cu-rich sample shows a maximum at 240 nm. Sample IE5 shows an additional peak around 390 nm.

Only one spin-allowed, Laporte-forbidden band is expected for Cu^{2+} species in octahedral sites, while three are expected for Ni^{2+} species:[22]

$$\begin{aligned} &\text{octahedral } Cu^{2+}(d^9) && {}^2E_g(D) \rightarrow {}^2T_{2g}(D) \\ &\text{octahedral } Ni^{2+}(d^8) && {}^3A_{2g}(F) \rightarrow {}^3T_{2g}(F) \\ & && {}^3A_{2g}(F) \rightarrow {}^3T_{1g}(F) \\ & && {}^3A_{2g}(F) \rightarrow {}^3T_{1g}(P) \end{aligned} \quad (3)$$

Taking into account the closeness between water and hydroxy ions in the spectrochemical series,[16] the broad band close to 770 nm is due to the ${}^2E_g(D) \rightarrow {}^2T_{2g}(D)$ transition of octahedral copper (*cf.* $[Cu(H_2O)_6]^{2+}$), with its broadness being due to distortion of its coordination from octahedral owing to the Jahn–Teller effect. For nickel containing samples, the peak corresponding to the transition ${}^3A_{2g}(F) \rightarrow {}^3T_{2g}(F)$ lies outside the spectral range of the instrument. The band corresponding to transition ${}^3A_{2g}(F) \rightarrow {}^3T_{1g}(F)$ splits because of spin–orbit coupling, and is usually found at 710–645 nm; finally, the transition ${}^3A_{2g}(F) \rightarrow {}^3T_{1g}(P)$ gives rise to a band at 390 nm.[22] The bands observed in the UV region (200–300 nm) are ascribed to charge transfer processes. These results indicate that the coordination of Ni^{2+} and Cu^{2+} ions should be close to that in the hexa-aqua complexes, confirming their location in the octahedral holes of the brucite-like layers.

Thermal analysis: DTA and TG

The DTA curves recorded for samples IE2–IE5 (Fig. 4) are typical of hydrotalcite-like materials.[19,23,24] The curve for sample IE3 (Fig. 4) shows a rather sharp endothermic effect at 177 °C, followed by a broader endothermic effect centered around 303 °C. Previous studies with Mg,Al hydrotalcites have shown[25–30] that the first peak corresponds to removal of

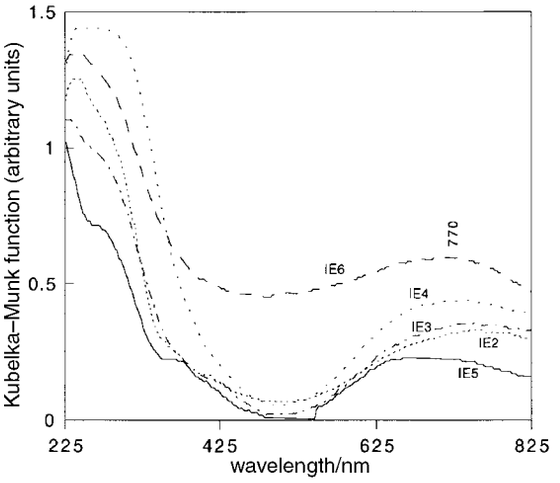

Fig. 3 UV–VIS/diffuse reflectance spectra for the samples studied. The curves have been displaced vertically for clarity.

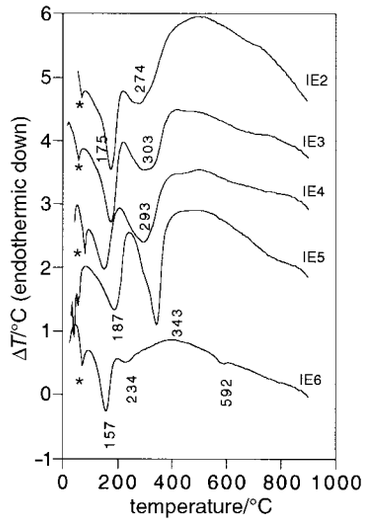

Fig. 4 Differential thermal analysis (DTA) curves for the samples studied. The curves have been displaced vertically for clarity; (*) instrumental artifacts.

interlayer water molecules, while the second effect combines removal of hydroxy groups from the brucite layers as water molecules, together with removal of interlayer carbonate anions as CO_2. The broadness of the second effect at 303 °C would account for this double process (water and carbon dioxide removal). The positions of these peaks shift slightly from one sample to another. Correspondingly, the TG curves (Fig. 5) show two overlapped weight losses whose inflection points, as determined from the DTG curves roughly coincide with those of the DTA minima.

The thermal behaviour shown by sample IE6 differs from that usually shown by hydrotalcites. It is noticeable the high temperature endothermic effect, recorded at 234 °C, is of significantly lower intensity than that of the first endothermic peak at 157 °C. Further, an additional endothermic peak is observed at 592 °C. For this sample, the TG curve (Fig. 5) shows a continuous weight loss and an additional weight loss fairly close to 600 ° (clearly detected in the DTG curve), a position coincident, within experimental error, with that of the 'unexpected' endothermic effect. This could probably arise from the presence of some carbonate ions strongly held to the brucite-like sheets. This behaviour has been previously

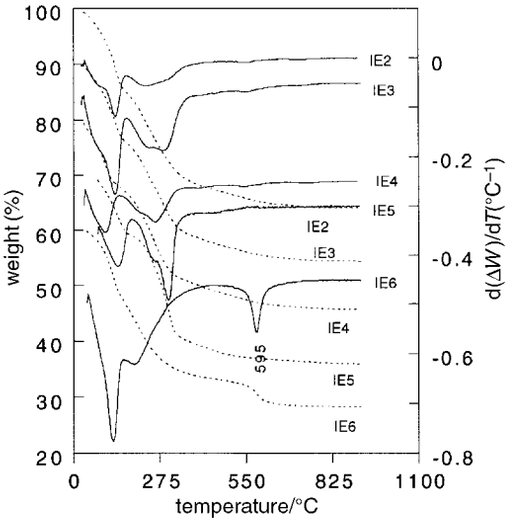

Fig. 5 Thermogravimetric analysis (TG, dotted lines) and differential thermogravimetric analysis (DTG, solid lines) curves for the samples studied. The curves have been displaced vertically for clarity.

reported for other copper containing hydrotalcite-like materials,[31–33] and is probably related to the large amount of copper present in this sample. In fact, to our knowledge, this high temperature thermal feature is unique for copper containing hydrotalcites.

Velu and Swamy[31] have observed this high temperature endothermic peak for Cu–Mn–Al hydrotalcite and using EGA (evolved gas analysis), found only CO_2 at that temperature. They have attributed this feature to some type of reaction occuring between brucite sheets and carbonate anions in the interlayer to form an oxycarbonate of chemical composition $[M^{II}M^{III}_xO_y(CO_3)_z]$ wherein the metal–oxygen bond remains intact and hence carbonate ions are substantially retained. More recently, Alejandre *et al.*[32] have attempted to synthesize pure Cu–Al hydrotalcite and found similar thermal features and attributed them to differences in the coordination behaviour of carbonate anion within the brucite lattice. In our opinion, the proposal of Velu and Swamy seems valid here, as we have not observed a significant split in the v_3 vibration mode of carbonate in the FTIR spectra, as seen by Alejandre *et al.*[32] An interesting point of observation is that, for pure copper containing hydrotalcites irrespective of its associated bivalent/trivalent metal ion, this thermal transformation occurs at 590–600 °C. In other words, the metastable phase, mainly amorphous, obtained during thermal treatment may be a pure copper containing oxycarbonate where the possibility of influence/presence of other metal ions is rather remote. Further, the temperature of this unusual endothermic peak is influenced significantly by the presence of impurity phases and copper content of the samples.

As mentioned above, the amount of interlayer water has been calculated from the weight losses recorded in the TG analysis and values are collected in Table 2. The maximum amount of water that can be acommodated in the interlayer of hydrotalcites can be calculated from the carbonate content. Assuming that a carbonate anion (in a 'flat' position, *i.e.*, with its molecular plane parallel to the brucite-like layers) occupies a volume three times that of a water molecule, and a close-packing of the interlayer species, for every two hydroxy groups in the brucite-like layers, a maximum of (2–3y) water molecules can be located in the interlayer space (y is the number of interlayer carbonate anions). The calculated values are always larger than the experimental ones; probably, hydrogen bonding in the interlayer, the existence of which has been already been confirmed from FTIR results, is responsible for the lower occupancy of the interlayer.

Temperature-programmed reduction (TPR)

Applicability of TPR to characterization of hydrotalcites has been reported elsewhere.[5,34] The analysis is not, however, straightforward, as the structure is being destroyed (see DTA–TG data above) while the layer cations are being reduced. TPR profiles are shown in Fig. 6 and in all cases, a sharp reduction maximum is recorded, followed by a broader, underlying, much weaker maximum. In the case of sample IE6 the sharp maximum shows a low temperature shoulder.

The precise positions of these maxima for all samples, as well as other quantitative data from the TPR study, are summarized in Table 3. The total amount of hydrogen consumed (Table 3) coincides well, within experimental error, with the expected value, assuming the reduction processes (Al^{3+} is not reduced under the experimental conditions used[34]):

$$Ni^{2+} + H_2 \rightarrow Ni^0 + 2H^+ \quad (4)$$

$$Cu^{2+} + H_2 \rightarrow Cu^0 + 2H^+ \quad (5)$$

Deviations between expected and measured H_2 consumption are not larger than 10% in any case. Further, the ratio between the integrated areas of the peaks roughly coincides with the

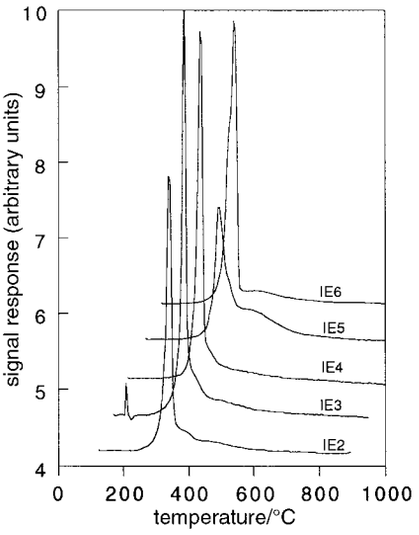

Fig. 6 Temperature-programmed reduction (TPR) curves for the samples studied. The curves have been displaced vertically and horizontally (+50 °C) for clarity.

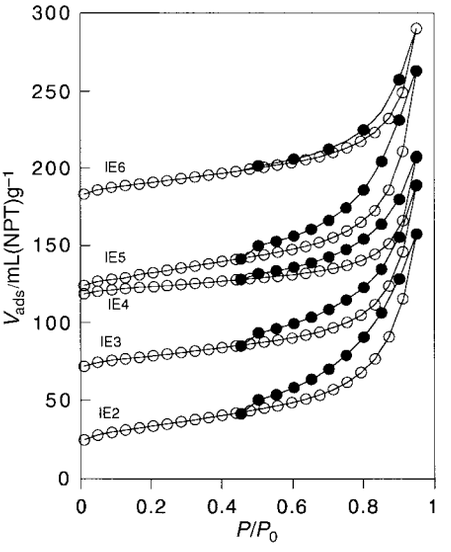

Fig. 7 Nitrogen adsorption–desorption isotherms (−196 °C) for the samples studied. The curves have been displaced vertically for clarity. (○) adsorption; (●) desorption.

ratio between the molar fractions of both cations. As in sample IE6 (that with the largest Cu^{2+} content) the first maximum is extremely intense, we can conclude that the sharp maximum is due to reduction of Cu^{2+} cations, while the second maximum arises from Ni^{2+} reduction. To confirm this experimentally, we have recorded TPR curves for some samples, up to the temperature just immediately after the first reduction peak, and also recorded the PXRD profile of the residue. These show exclusively the diffraction lines of Cu (JCPDS file 4-0836) substantiating the above conclusion. Moreover, while reduction of Cu^{2+} is complete at *ca.* 300 °C, it is necessary to heat the samples to above 450–500 °C to achieve complete reduction of Ni^{2+} species.

A closer look at the reduction temperature for nickel, T_2 (Table 3) for samples IE2–IE4 indicated a decrease in its value with an increase in aluminium content. This may be due to dissolution of more aluminium in an '*in situ*' generated NiO lattice (rock-salt structure) to form a solid solution thereby hindering the reducibility of nickel. Similar observations were made previously by Clause *et al.*,[35] for Ni–Al hydrotalcites by invoking a 'decorated' three phase model. Further, T_1 (reduction temperature of copper) was not affected significantly by the variation in nickel or aluminium content. In other words, there is a facile thermodynamic nucleation and growth of '*in situ*' generated CuO islands preventing the diffusion of Al^{3+} thereby avoiding the possibility of formation of such solid solutions. A weak shoulder observed for IE6 corroborates the Jahn–Teller influence on copper wherein copper may possibly be present in two different symmetric environments.

Surface texture

Nitrogen adsorption–desorption isotherms for all five samples (IE2–IE6) are plotted in Fig. 7. The curves belong to type II in the IUPAC classification,[36] and show a hystheresis loop closing at *ca.* 0.45 (P/P_0). These curves indicate that all samples are mesoporous, without micropores, *i.e.*, the nitrogen molecules are unable to penetrate the interlayer space of the hydrotalcites. The *t*-plots[37] lead in all cases to straight lines passing through the origin of the *V*–*t* plot upon extrapolation, confirming the absence of micropores measurable by N_2 adsorption. The pore size distribution curves show in all cases a bimodal curve, with a maximum contribution by pores with a diameter close to 35 Å, and an underlying contribution by pores with diameters of 40–60 Å. The values for the specific surface areas, as calculated following the BET method (s_{BET}), are given in Table 4, together with the total pore values.

Characterisation of calcined products

Although hydrotalcites themselves are materials of worthwhile study, in many cases they are used as catalyst precursors. In a hydrotalcite the cations are homogeneously distributed and, upon calcination, well dispersed mixed oxides are usually

Table 4 Summary of specific surface areas and porosities

Sample	S_{BET}[a]/m^2 g^{-1}	V_p[b]
IE2	105	0.29
IE3	77	0.24
IE4	50	0.17
IE5	87	0.26
IE6	89	0.23
IE2-500	123	0.32
IE3-500	122	0.36
IE4-500	105	0.33
IE5-500	167	0.46
IE6-500	90	0.31

[a]Specific surface area. [b]Total pore volume, ml liquid N_2 g^{-1}.

Table 3 Summary of TPR results

Sample	H_2[a]	(Ni+Cu)[b]	T_1[c]/°C	T_2[c,d]/°C	A_2/A_1[e]
IE2	6550	6184	270	293	0.70
IE3	7396	6724	266	280	0.93
IE4	7457	7415	268	271	0.72
IE5	7576	6849	275	327	4.17
IE6	7599	6922	265	315	0.25

[a]μmol H_2 consumed/g sample. [b]μmol (Cu+Ni)/g sample. [c]Temperature of the maxima. [d]±10 °C. [e]Ratio between integrated areas of the sharp and broad peak (see text).

obtained and of higher quality than when starting from the pure oxides separately.

In this study, the samples were calcined in air at 500 °C for 2 h (heating rate up to 500 °C was 10 °C min^{-1}), *i.e.*, just after the main endothermic effects. In addition, samples IE4 and IE6 were also calcined at 850 °C, in order to identify the origin of the thermal effects recorded at high temperature. The samples are denoted IEX-T, where T is the calcination temperature, in °C.

Powder X-ray diffraction

PXRD patterns for the calcined samples are shown in Fig. 8. As already reported for other hydrotalcites,[19,38,39] calcination at this 'intermediate' temperature gives rise to mostly amorphous solids, with rather weak, broad diffraction peaks. In our case, three peaks are recorded close to 2.42, 2.07 and 1.47 Å, positions coincident with the main diffraction maxima of bunsenite (NiO, JCPDS file 4-0835). However, for sample IE6, in addition, sharper maxima are also recorded, whose positions coincide with those of tenorite (CuO, JCPDS file 5-0661); it should be noted that sample IE6 is that with the highest copper content, while for the other samples the Cu content slightly exceeds that of nickel. In the other samples the maxima arising from CuO (if existing) should be included in the broad tails of the main peaks of NiO. The change in the relative intensities of the peaks recorded close to 2.42 and 2.07 Å ($2\theta = 36$ and 43°, respectively) is undoubtedly due to the change in the relative content of Ni and Cu. Jobbágy *et al.*[40] have reported the presence (as evidenced by X-ray diffraction) of bunsenite as a single crystalline phase, when Cu^{2+} ions are dissolved up to a copper concentration of $x = 0.35$, upon calcination of a $Ni_{1-x}Cu_x(OH)_2$ precursor, without formation of any discrete Cu-containing phase. This is in contrast to our findings, where CuO segregates as a discrete phase, probably as a consequence of the variation in the preparation methodology.

In our case, no peak was recorded which could be ascribed to Al-containing phases. This is not unexpected, as usually at 400–500 °C only the diffraction peaks of the divalent metal oxide are recorded, although the positions do not exactly match those reported for the pure oxides, and so it is generally assumed that Al^{3+} cations are dissolved in the $M^{II}O$ matrix; when the calcination temperature is increased (850–1000 °C), crystallization of the $M^{II}Al_2O_4$ spinel is usually observed.

PXRD patterns for samples calcined at 850 °C are shown in Fig. 9 and crystallization of well defined phases can be observed. All peaks recorded can be ascribed to the presence of tenorite (CuO), bunsenite (NiO) or $NiAl_2O_4$ spinel (JCPDS file 10-0339). No difference between the nature of the crystalline phases can be seen for the different samples,

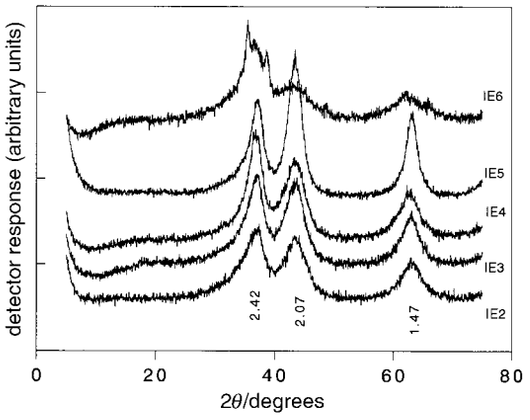

Fig. 8 Powder X-ray diffraction patterns for the samples calcined at 500 °C. The curves have been displaced vertically for clarity. Positions marked (Å) correspond to averaged values.

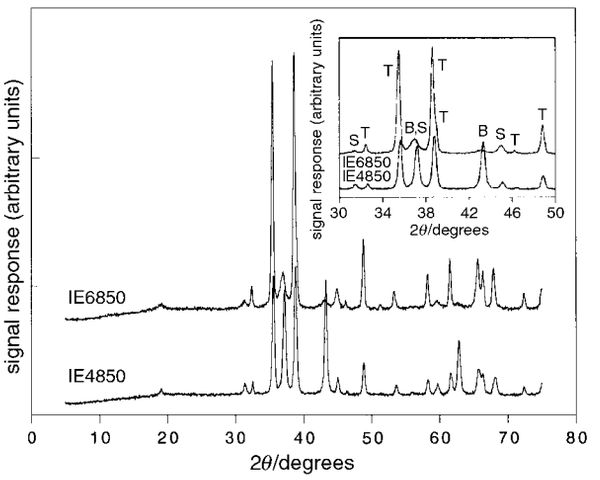

Fig. 9 Powder X-ray diffraction patterns for the samples calcined at 850 °C. Inset: $30 \leqslant 2\theta \leqslant 50°$. The curves have been displaced vertically for clarity. B = bunsenite (NiO); S = spinel ($NiAl_2O_4$); T = tenorite (CuO).

although differences exist in the relative intensities of the corresponding maxima, in agreement with the relative content of the different metal cations. For sample IE6-850, with the largest Cu content, the main diffraction maxima recorded correspond to CuO while for sample IE4-850 the main peaks are due to both CuO and NiO.

Specific surface area and porosity assessment

Specific surface areas and total pore volumes for all five samples calcined at 500 °C are included in Table 4. For all samples, except for IE6-500, an increase in both variables is observed upon calcination, compared to the values for the uncalcined samples. This can be explained[18] assuming that removal of water and CO_2 during calcination leads to formation of channels and pores (chimneys), thus accounting for the increase in specific surface area. By contrast, the specific surface area for sample IE6-500 coincides, within experimental error, with that for the uncalcined sample, despite the fact that they display different PXRD patterns. This behavior is probably simply a coincidence; the rather 'low' value for sample IE6-500 may be due to incipient crystallization of CuO, as shown by the PXRD patterns.

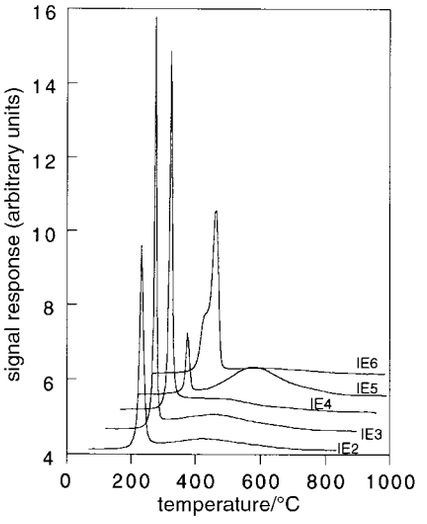

Fig. 10 Temperature-programmed reduction (TPR) curves for the samples calcined at 500 °C. The curves have been displaced vertically and horizontally (+50 °C) for clarity.

Temperature-programmed reduction

TPR curves for samples calcined at 500 °C are shown in Fig. 10 and are similar to those obtained for the corresponding uncalcined samples. However, a detailed analysis of the curves indicates that, while the maximum assigned to reduction of copper is recorded at the same position, the broad maximum ascribed to reduction of Ni^{2+} shifts towards higher temperatures in all cases. In other words, Ni^{2+} species are more difficult to reduce in the calcined samples. This is probably due to slow diffusion of Al^{3+} cations into an '*in situ*' generated NiO matrix (kinetic control) with an increasing temperature during TPR of the fresh sample, while the same process is facilitated through prior calcination resulting in a well defined Ni–Al oxide solid solution, thereby preventing the accessibility of the reducing molecules to the nickel oxide surface.[5]

Conclusions

In the present study, we have prepared materials with hydrotalcite-like structures, differing in the relative amounts of Cu, Ni and Al in the brucite-like layers. In all cases where $M^{II}/M^{III} \geqslant 2$, the hydrotalcite structure is formed. The presence of a large excess of Al^{3+} in sample IE1 leads to formation, in addition to a hydrotalcite-like phase, of gibbsite.

The nature of phase obtained, crystallinity of the HT-like phase formed and the thermal behaviour of these materials were significantly influenced by the nature and concentrations of the different metals.

An unusual endothermic peak is observed for the Cu-rich hydrotalcite, probably owing to the formation of a metastable amorphous copper oxycarbonate phase. Interestingly, we observe that the temperature of this endotherm is nearly the same for all Cu-containing pure hydrotalcites irrespective of the nature of other metal ions present in the sample.

Calcination at 850 °C leads to crystallization of well defined phases, the nature of which is in agreement with the major components of the solids: NiO and CuO in sample IE4, and CuO in sample IE6.

Acknowledgements

V.R. thanks Junta de Castilla y León (Consejería de Educación y Cultura, ref. SA45/96), CICYT (IN96-0252), and DGESIC (grant PB96-1307-C03-01) for financial support and Mr. A. Montero for TPR and FT-IR measurements. S.K. acknowledges Dr S. D. Gomkale (Acting Director, CSMCRI, India) for permitting this collaborative research work.

References

1 F. Cavani, F. Trifirò and A. Vaccari, *Catal. Today*, 1991, **11**, 173 and references therein.
2 A. De Roy, C. Forano, K. El Malki and J. P. Besse, in *Expanded Clays and Other Microporous Solids, Synthesis of Microporous Materials*, ed. M. L. Occelli and H. Robson, van Nostrand Reinhold, New York, 1992, ch. 7, p. 108 and references therein.
3 F. Trifirò and A. Vaccari, in *Comprehensive Supramolecular Chemistry*, ed. J. L. Atwood, J. E. D. Davies, D. D. MacNicol, F. Vögtle, J.-M. Lehn, G. Alberti and T. Bein, Pergamon-Elsevier Science, Oxford, 1996, vol. 7, p. 251 and references therein.
4 V. Rives and M. A. Ulibarri, *Coord. Chem. Rev.*, 1999, **181**, 61 and references therein.
5 D. Tichit, F. Medina, B. Coq and R. Dutartre, *Appl. Catal. A: Gen.*, 1997, **159**, 241.
6 V. Rives, F. M. Labajos, R. Trujillano, E. Romeo, C. Royo and A. Monzón, *Appl. Clay Sci.*, 1998, **13**, 363.
7 S. Kannan, A. Narayanan and C. S. Swamy, *J. Mater. Sci.*, 1996, **31**, 2353.
8 K. Zhu, C. Liu, X. Ye and Y. Wu, *Appl. Catal. A: Gen.*, 1998, **168**, 365.
9 F. Kooli, V. Rives and W. Jones, *Chem. Mater.*, 1997, **9**, 2231.
10 JCPDS: Joint Committee on Powder Diffraction Standards, International Centre for Diffraction Data, Swarthmore, PA, 1977.
11 P. Malet and A. Caballero, *J. Chem. Soc., Faraday Trans. 1*, 1988, **84**, 2369.
12 V. Rives, *Adsorption Sci. Technol.*, 1991, **8**, 95.
13 A. S. Bookin and A. Drits, *Clays Clay Miner.*, 1993, **41**, 551.
14 A. S. Bookin, V. I. Cherkashin and A. Drits, *Clays Clay Miner.*, 1993, **41**, 558.
15 M. A. Drezdzon, *Inorg. Chem.*, 1988, **27**, 4628.
16 J. E. Huheey, E. A. Keiter and R. L. Keiter, *Inorganic Chemistry: Principles of Structure and Reactivity*, Harper Collins College, Publishers, New York, 4th edn., 1993.
17 M. J. Hernández-Moreno, M. A. Ulibarri, J. L. Rendón and C. J. Serna, *Phys. Chem. Miner.*, 1985, **12**, 34.
18 E. C. Kruissink, L. J. van Reijden and J. R. H. Ross, *J. Chem. Soc., Faraday Trans. 1*, 1981, **77**, 649.
19 F. M. Labajos, V. Rives and M. A. Ulibarri, *J. Mater. Sci.*, 1992, **27**, 1546.
20 V. Rives-Arnau, G. Munuera and J. M. Criado, *Spectrosc. Lett.*, 1979, **12**, 733.
21 K. Nakamoto, *Infrared and Raman Spectra of Inorganic and Coordination Compounds*, J. Wiley & Sons, New York, 4th edn., 1986.
22 A. B. P. Lever, *Inorganic Electronic Spectroscopy*, Elsevier, Amsterdam, 2nd edn., 1984.
23 L. Pesic, S. Salipurovic, V. Markovic, D. Vucelic, W. Kagunya and W. Jones, *J. Mater. Chem.*, 1992, **2**, 1069.
24 M. J. Hernández, M. A. Ulibarri, J. L. Rendón and C. J. Serna, *Themochim. Acta*, 1984, **81**, 311.
25 D. L. Bish and G. W. Brindley, *Am. Mineral.*, 1977, **62**, 458.
26 T. Sato, K. Kato, T. Endo and M. Shimada, *React. Solids*, 1986, **2**, 253.
27 T. Sato, T. Wakabayashi and M. Shimada, *Ind. Eng. Chem. Prod. Res. Dev.*, 1986, **25**, 89.
28 M. del Arco, C. Martín, I. Martín, V. Rives and R. Trujillano, *Spectrochim. Acta, Part A*, 1993, **49**, 1575.
29 V. Rives, *Inorg. Chem.*, 1999, **38**, 406.
30 A. M. Aicken, I. S. Bell, P. V. Coveney and W. Jones, *Adv. Mater.*, 1997, **9**, 496.
31 S. Velu and C. S. Swamy, *J. Mater. Sci. Lett.*, 1996, **15**, 1674.
32 A. Alejandre, F. Medina, P. Salagre, X. Correig and J. E. Sueiras, *Chem. Mater.*, 1999, **11**, 939.
33 M. J. L. Gines and C. R. Apestiguia, *J. Therm. Anal.*, 1997, **50**, 745.
34 V. Rives, M. A. Ulibarri and A. Montero, *Appl. Clay Sci.*, 1995, **10**, 83.
35 B. Rebours, J. B. d'Espinose de la Caillerie and O. Clause, *J. Am. Chem. Soc.*, 1994, **116**, 1707.
36 K. S. W. Sing, D. H. Everett, R. A. W. Haul, L. Moscou, E. Pierotti, J. Rouquerol and T. Sieminiewska, *Pure Appl. Chem.*, 1985, **57**, 603.
37 B. C. Lippens and J. H. de Boer, *J. Catal.*, 1965, **4**, 319.
38 M. del Arco, M. V. G. Galiano, V. Rives, R. Trujillano and P. Malet, *Inorg. Chem.*, 1996, **35**, 6362.
39 M. del Arco, V. Rives, R. Trujillano and P. Malet, *J. Mater. Chem.*, 1996, **6**, 1419.
40 M. Jobbágy, G. J. A. A. Soler-Illia, A. E. Regazzoni and M. A. Blesa, *Chem. Mater.*, 1998, **10**, 1632.

Paper a908534c